

Metalated Diblock and Triblock Poly(ethylene oxide)-*block*-poly(4-vinylpyridine) Copolymers: Understanding of Micelle and Bulk Structure

Lyudmila M. Bronstein,^{*,†} Stanislav N. Sidorov,[‡] Vasilii Zhironov,[‡] Denis Zhironov,[‡] Yuri A. Kabachii,[‡] Sergey Y. Kochev,[‡] Peter M. Valetsky,[‡] Barry Stein,[†] Olga I. Kiseleva,[§] Sergey N. Polyakov,[§] Eleonora V. Shtykova,^{||} Elena V. Nikulina,^{||} Dmitri I. Svergun,^{||,⊥} and Alexei R. Khokhlov[§]

Department of Chemistry, Indiana University, 800 East Kirkwood Avenue, Bloomington, Indiana 47405, A.N. Nesmeyanov Institute of Organoelement Compounds, 28 Vavilova Street, 119991 Moscow, Russia, Physics Department, Moscow State University, GSP-2, Leninskiye Gory, 119992 Moscow, Russia, Institute of Crystallography, Russian Academy of Sciences, 14 Leninskii pr. 59, 117333 Moscow, Russia, and European Molecular Biology Laboratory, Hamburg Outstation, Notkestrasse 85, D-22603 Hamburg, Germany

Received: June 21, 2005; In Final Form: August 11, 2005

The paper provides new insights into the structure of Pt-containing diblock and triblock copolymers based on poly(ethylene oxide) (PEO) and poly(4-vinylpyridine) (P4VP), using a combination of atomic force microscopy (AFM), X-ray diffraction (XRD), transmission electron microscopy (TEM), and anomalous small-angle X-ray scattering (ASAXS). Parallel studies using methods contributing supplemental structural information allowed us to comprehensively characterize sophisticated polymer systems during metalation and to exclude possible ambiguity of the data interpretation of each of the methods. AFM and TEM make available the determination of sizes of the micelles and of the Pt-containing micelle cores, respectively, while a combination of XRD, TEM, and ASAXS reveals Pt-nanoparticle size distributions and locations along with the structural information about the polymer matrix. In addition, for the first time, ASAXS revealed the organization of Pt-nanoparticle-filled diblock and triblock copolymers in the bulk. The nanoparticle characteristics are mainly determined by the type of block copolymer system in which they are found: larger particles (2.0–3.0 nm) are formed in triblock copolymer micelles, while smaller ones (1.5–2.5 nm) are found in diblock copolymer micelles. This can be explained by facilitated intermicellar exchange in triblock copolymer systems. For both systems, Pt nanoparticles have narrow particle size distributions as a result of a strong interaction between the nanoparticle surface and the P4VP units inside the micelle cores. The pH of the medium mainly influences the particle location rather than the particle size. A structural model of Pt-nanoparticle clustering in the diblock PEO-*b*-P4VP and triblock P4VP-*b*-PEO-*b*-P4VP copolymers in the bulk was constructed *ab initio* from the ASAXS data. This model reveals that nearly spherical micellar cores of about 10 nm in diameter (filled with Pt nanoparticles) aggregate forming slightly oblate hollow bodies with an outer diameter of about 40 nm.

Introduction

Amphiphilic block copolymers form micelles in selective solvents (a good solvent only for one block), yet the size and shape of micelles depend on the block chemical structure, molecular weight of each block, and solvent type.^{1–7} The formation of metal, metal oxide, and metal chalcogenide nanoparticles in block copolymer micelles has received considerable attention as a result of their unique properties. Block copolymer micelles filled with nanoparticles displayed exceptional catalytic,^{8–12} magnetic,^{13–15} and optical^{16,17} properties and were used for nanolithography,¹⁸ for improvement of tribological performance of mineral oil,¹⁹ and in biological and pharmaceutical applications.^{20,21} If the block containing the functional groups forms the micelle core, it can be loaded with a corresponding metal compound and serve as a nanoreactor for nanoparticle formation and stabilization. Because the core-forming block is

not soluble in a selective solvent, the micelle core can be treated like a quasi-solid, thus, additionally stabilizing the nanoparticles. A block containing no functional groups but providing solubility and micelle stability in the solution should form the micelle corona.

The synthesis of metal or semiconductor nanoparticles in the cores of amphiphilic block copolymer micelles in organic solvents was reported by many research groups.^{19,22–27} Using block copolymer micelle cores as nanoreactors allows the synthesis of mono- and bimetallic nanoparticles, yet bimetallic particle morphology depends on a metal pair, that is, on the relative ability of the metal species to be reduced in the particular conditions.⁹ These different morphologies significantly change the catalytic properties of such systems, although the nanoparticle sizes are similar. When block copolymer micelles are cross-linked, this provides an additional degree of stabilization to nanoparticles and allows the modification of micelle morphology.^{28–30} The possibility of using such nanospheres as nanoreactors for inorganic nanoparticles was demonstrated by the formation of iron oxide magnetic particles³⁰ and catalytic Pd nanoparticles.²⁹ The spatial distribution of nanoparticles in block

* To whom correspondence should be addressed: lybronst@indiana.edu.

† Indiana University.

‡ A.N. Nesmeyanov Institute of Organoelement Compounds.

§ Moscow State University.

|| Russian Academy of Sciences.

⊥ European Molecular Biology Laboratory.

copolymers was also extensively studied by a number of research groups.^{31–35} The selective separation of nanoparticles between blocks was achieved as a result of the presence of functional groups in a selected block.

Large numbers of amphiphilic block copolymers form micelles with a functionalized core in the organic medium. When aqueous solutions are favored (from the environmental point of view or for particular applications), the choice of block copolymers is very limited, and nanoparticle formation is normally more complicated as the pH of the medium should be taken into consideration. A few examples of such block copolymers include poly(ethylene oxide)-*block*-poly(2-vinylpyridine) (PEO-*b*-P2VP),³⁶ polybutadiene-*block*-poly(ethylene oxide) (PB-*b*-PEO),³⁷ polystyrene-*block*-poly(2-vinylpyridine)-*block*-poly(ethylene oxide) (PS-*b*-P2VP-*b*-PEO),³⁸ and poly-[methoxyhexa(ethylene glycol) methacrylate]-*block*-[2-(diethylamino)ethyl methacrylate] (PHEGMA-*b*-PDEAEMA).³⁹ When the core-forming block is pH sensitive (such as P2VP or PDEAEMA), micellization depends on pH.⁴⁰ For example, at a pH below 5, PEO-*b*-P2VP forms a molecular solution in water, whereas a decrease of pH of the PEO-*b*-P2VP micellar solution after the incorporation of metal compounds or metal nanoparticle formation results in no micelle decomposition as a result of the interaction with metal species.³⁶

The formation of spherical assemblies of CdS-containing block copolymer reverse micelles in aqueous solution was reported in ref 41. These stable assemblies were formed by the slow addition of water to mixtures of the reverse micelles formed by PS-*b*-PAA [PAA stands for poly(acrylic acid)] and single PS-*b*-PAA chains. This resulted in large compound micelles containing quantum-confined CdS nanoparticles. This method allows the transferring of the CdS nanoparticles formed in the micelle cores in organic medium to aqueous medium without the loss of stability or nanoparticle aggregation.

For the templating of platinum nanoparticles, in this work we have chosen poly(ethylene oxide)-*block*-poly(4-vinylpyridine) (PEO-*b*-P4VP) prepared by atom transfer radical polymerization (ATRP) using a PEO macroinitiator. This method is cheaper and more robust compared to anionic polymerization, which is used for the synthesis of PEO-*b*-P2VP.³⁶ The choice of P4VP as the core-forming block allows easy coordination with a wide range of metal ions.⁴² As was reported,⁴³ the interaction between P4VP and metal compounds is less sterically hindered compared to that of P2VP, thus, P4VP should result in more stable nanoparticles. In our preceding publication we reported the formation of gold nanoparticles in the diblock PEO-*b*-P4VP copolymer.⁴⁴ This paper describes micellar characteristics and Pt-nanoparticle formation in the diblock PEO-*b*-P4VP and triblock P4VP-*b*-PEO-*b*-P4VP micelles using a combination of transmission electron microscopy (TEM), atomic force microscopy (AFM), X-ray diffraction (XRD), and anomalous small-angle X-ray scattering (ASAXS). Each of the methods provides valuable structural information, and their simultaneous use gives comprehensive insights into the organization of complicated polymer systems. Moreover, each technique has both its intrinsic capabilities and its inherent limitations. Among these methods, ASAXS has particular significance.

For the development of novel nanomaterials with special properties, the problem of nondestructive quantitative analysis of structural characteristics determining the properties of the materials is very important. Small-angle X-ray scattering (SAXS) is a diffraction method widely and successfully employed to analyze the structure of various disperse systems at resolutions from about 1 to 100 nm.^{45–49} The SAXS patterns

provide structural information both about nanoscale inhomogeneities (particles or clusters) and about the internal ordering in the sample.⁵⁰ The size and shape of the nanoparticles can be assessed from the portion of the scattering pattern close to the primary beam (central scattering). When studying metal nanoparticles in nanostructured polymer matrices, ASAXS is of special importance because it allows one to separate and analyze scattering contributions from the metal nanoparticles and their polymer environment,^{51,52} similar to other metal-containing composite materials.^{53–55} An examination of these contributions permits the calculation of the volume distribution functions of the metal nanoparticles from the central scattering and the determination of the internal structure of the polymer using information contained in the characteristic Bragg peaks at higher scattering angles.^{56–59} Furthermore, recently developed methods⁶⁰ allow one to determine the ab initio low-resolution structure of particles.^{61–64} In the present paper, ab initio modeling together with the comprehensive analysis of the ASAXS profiles is applied for the first time to reveal the structural model of Pt-nanoparticle organization in the diblock PEO-*b*-P4VP and triblock P4VP-*b*-PEO-*b*-P4VP copolymers in the bulk, which is compatible with the results of TEM, AFM, and XRD. In addition, here we present the first example when, in block copolymer micelles, nanoparticle size is independent of the reducing-agent type (similar to nanoparticle growth in a confined environment), which is attributed to a strong interaction of the vinyl pyridine units with the growing nanoparticle surface in the micelle cores cross-linked with platinum acid.

Experimental Section

Materials. CH₂Cl₂ (99.6%, Aldrich) was purified by shaking it with a small amount of H₂SO₄ twice until the acid remained nearly colorless. Then CH₂Cl₂ was washed with water (twice), then with a 5% solution of NaHCO₃, and then again with water (twice) and then left over anhydrous CaCl₂ overnight. CH₂Cl₂ was then mixed with CaH₂ for 1 h, boiled for 2 h, and distilled over CaH₂. Toluene (99.5%, Aldrich) was kept over CaCl₂ overnight and then distilled. H₂PtCl₆·6H₂O (Reakhim, Russia) and hydrazine hydrate (N₂H₄·H₂O, 98+%, Aldrich) were used as received.

PEO monomethyl ether ($M_n = 2000$ g/mol, Aldrich) and poly(ethylene glycol) (PEG, $M_n = 12\,000$ g/mol, Fluka) were dehydrated by the distillation of the water as the azeotrope with toluene. For this, PEO and PEG were mixed with toluene (7 mL of toluene/1 g of polymer) and distilled at 125–130 °C. After the evaporation of the toluene, the polymers were dried under vacuum at 65 °C for 1 h. The products were stored under argon.

4-Vinylpyridine (4VP, Aldrich) was stirred with a small amount of CaH₂ at 40–50 °C for 2 h. Then 4VP was decanted, degassed via three freeze–thaw cycles, and distilled under vacuum into a Schlenk tube. The Schlenk tube containing the 4VP was filled with argon and was stored in a refrigerator at –15 °C. 2-Propanol (*i*-PrOH) was purified in a similar manner as that used for 4VP and stored under argon at room temperature. 2-Chloropropionyl chloride (97%, Aldrich), triethylamine (TEA, >99.5%, Fluka), and CuCl (98+%, Aldrich) were used as received. Tris(2-dimethylaminoethyl)amine (Me₆TREN) was obtained as described elsewhere.⁶⁵

Synthesis. Modification of PEO and PEG with 2-Chloropropionyl Groups. PEO and PEG with 2-chloropropionyl terminated groups (PEO-CP, CP-PEG-CP) were prepared using a modified version of the technique described by Jankova et al.⁶⁶ The modification consisted of the use of only TEA as the

HCl absorber. CP-PEG-CP would not crystallize in ethanol; therefore, it was purified by a triple extraction of the polymer powder with ethanol (7 mL ethanol/1 g of polymer, 2 h at room temperature). The completeness of the terminal group modification and the purity of the polymers were monitored by ^1H NMR. No polymer chain destruction was observed.

Synthesis of Diblock PEO-*b*-P4VP. The PEO-*b*-P4VP block copolymer was synthesized by the ATRP of 4VP with a PEO-CP macroinitiator using an approach described by Matyjaszewski et al.⁶⁷ In a typical procedure, a Schlenk tube equipped with a magnetic stir bar was loaded with 0.107 g (1.08 mmol) of CuCl, 4.54 g (43.2 mmol) of 4VP, and 0.249 g (1.08 mmol) of Me₆TREN, degassed via three freeze–thaw cycles, and stirred at 25 °C until there was complete dissolution of CuCl. Then, using a degassed syringe, this mixture was added to a Schlenk tube containing a degassed solution of PEO-CP (2.88 g, 44 mmol) in 9.6 mL of *i*-PrOH in argon counterflow at 40 °C under vigorous stirring. The homogeneous mixture was placed in a bath at 50 °C, stirred for 8 h, and kept overnight at room temperature. The Schlenk tube content was then dissolved in 50 mL of tetrahydrofuran (THF), and the 4VP conversion was evaluated by gas chromatography (95%). The solution was filtered through Al₂O₃ powder to remove the Cu complex, and the THF was distilled off until a residual volume of 20 mL remained. The polymer was precipitated in diethyl ether and dried under vacuum at 40 °C for 5 h. The yield was 5.6 g (76%). The number-average degree of polymerization of the P4VP blocks was determined from the degree of polymerization of the PEO (45) using ^1H NMR (CDCl₃). In the resulting PEO-*b*-P4VP copolymer, the molecular weight of the P4VP block was 2940; that is, the degree of polymerization was 28.

Synthesis of P4VP-*b*-PEO-*b*-P4VP. In a typical experiment, a Schlenk tube equipped with a magnetic stir bar was loaded with 0.45 g (4.55 mmol) of CuCl, 18.20 g (0.173 mol) of 4VP, and 1.00 g (1.08 mmol) of Me₆TREN, degassed via three freeze–thaw cycles, and stirred at 25 °C until there was complete dissolution of CuCl. Then, using a degassed syringe, this mixture was added to a degassed solution of CP-PEG-CP (26.00 g, 4.33 mmol) in a mixture of 22 mL of *i*-PrOH and 22 mL of toluene and placed in the Schlenk tube in argon counterflow at 40 °C under vigorous stirring. The homogeneous solution was stirred at 50 °C for 16 h. The Schlenk tube content was then dissolved in 500 mL of THF, and the 4VP conversion was evaluated by gas chromatography (86%). The solution was filtered through Al₂O₃ powder to remove the Cu complex, and the THF was distilled off until a residual volume of 200 mL remained. The polymer was precipitated in diethyl ether and dried under vacuum at 40 °C for 5 h. The yield was 35.0 g (79%). The number-average degree of polymerization of the P4VP blocks was determined from the degree of polymerization of the PEG (273) using ^1H NMR (CDCl₃). In the resulting P4VP-*b*-PEG-*b*-P4VP copolymer, the molecular weight of the P4VP blocks was 3050; that is, the degree of polymerization was 29.

Metalation of PEO₄₅-*b*-P4VP₂₈ Micelles. PEO₄₅-*b*-P4VP₂₈-Pt (NaBH₄), pH = 2. In a typical experiment for PEO₄₅-*b*-P4VP₂₈, 0.1 g of a block copolymer was dissolved in 30 mL of water and stirred for 2 days. H₂PtCl₆·6H₂O (0.0962 g, 1.86 × 10⁻⁴ mol) was added to the PEO₄₅-*b*-P4VP₂₈ solution and stirred for 2 days. Then, the solution was ultrafiltered with an Amicon ultrafiltration device, degassed to remove oxygen, and reduced in an argon atmosphere with 5-fold molar excess of NaBH₄ (0.0353 g, 9.3 × 10⁻⁴ mol). For PEO₄₅-*b*-P4VP₂₈-Pt (NaBH₄), pH = 10, the same procedure was used, except that,

after the addition of platinum acid, the pH of the reaction solution was adjusted to 10 before reduction. An excess of water was removed by ultrafiltration. For PEO₄₅-*b*-P4VP₂₈-Pt (N₂H₄), pH = 10, 5-fold molar excess of N₂H₄·H₂O (0.446 mL of a 10% aqueous solution, 9.3 × 10⁻⁴ mol) was used instead of NaBH₄. For PEO₄₅-*b*-P4VP₂₈-Pt (NaBH₄ + N₂H₄), pH = 10, two reducing agents were used. First, in an argon atmosphere, NaBH₄ (0.0106 g, 2.8 × 10⁻⁴ mol) was added, and then, after 30 min, the solution was additionally reduced with N₂H₄·H₂O (0.314 mL of a 10% aqueous solution, 6.5 × 10⁻⁴ mol). For PEO₄₅-*b*-P4VP₂₈-Pt (N₂H₄ + NaBH₄), pH = 10, 0.134 mL of a 10% N₂H₄·H₂O aqueous solution (2.8 × 10⁻⁴ mol) was added first followed by 2.47 × 10⁻² g (6.5 × 10⁻⁴ mol) of NaBH₄.

P4VP₂₉-*b*-PEO₂₇₂-*b*-P4VP₂₉-Pt (NaBH₄), pH = 2. In a typical experiment for P4VP₂₉-*b*-PEO₂₇₂-*b*-P4VP₂₉, 0.1 g of a triblock copolymer was dissolved in 100 mL of water and stirred for 2 days. Then H₂PtCl₆·6H₂O (0.0565 g, 1.1 × 10⁻⁴ mol) was added to the P4VP₂₉-*b*-PEO₂₇₂-*b*-P4VP₂₉ solution and stirred for 2 days. After ultrafiltration, a degassed reaction solution was reduced in an argon atmosphere with 5-fold molar excess of NaBH₄ (0.021 g, 5.5 × 10⁻⁴ mol). For P4VP₂₉-*b*-PEO₂₇₂-*b*-P4VP₂₉-Pt (NaBH₄), pH = 10, the same procedure was used, except that, after the H₂PtCl₆·6H₂O addition, the pH of the reaction solution was adjusted to 10 with 0.1 N NaOH. An excess of water was removed by ultrafiltration. For P4VP₂₉-*b*-PEO₂₇₂-*b*-P4VP₂₉-Pt (N₂H₄), pH = 10, a 5-fold molar excess of N₂H₄·H₂O (0.264 mL of a 10% aqueous solution, 5.5 × 10⁻⁴ mol) was used instead of NaBH₄. For P4VP₂₉-*b*-PEO₂₇₂-*b*-P4VP₂₉-Pt (NaBH₄ + N₂H₄), pH = 10, two reducing agents were used. First, in an argon atmosphere, NaBH₄ (0.0063 g, 1.65 × 10⁻⁴ mol) was added, and then, after 30 min, the solution was treated with N₂H₄·H₂O (0.184 mL of a 10% aqueous solution). For P4VP₂₉-*b*-PEO₂₇₂-*b*-P4VP₂₉-Pt (N₂H₄ + NaBH₄), pH = 10, 0.079 mL of a 10% aqueous solution (1.65 × 10⁻⁴ mol) of N₂H₄·H₂O was added first, followed by 0.0146 g (3.85 × 10⁻⁴) mol of NaBH₄.

Characterization. Specimens for TEM were prepared either by placing a drop of solution onto a carbon-coated copper grid or by sectioning an epoxy-embedded specimen. In the latter case, the polymer powder was prepared by crushing the films obtained after water evaporation from the micellar solutions using a mortar and pestle. Images were acquired at an accelerating voltage of 60 kV on a JEOL JEM1010.

AFM experiments were performed in tapping mode using the Nanoscope IIIa (Digital Instruments, U.S.A.) multimode scanning probe microscope. Commercially available standard silicon 125-μm tapping mode cantilevers (Nanoprobe) were used. The resonant frequency was in the interval of 300–350 kHz, and the scan rate was maintained at 1.5–2.0 Hz. The samples were applied onto a freshly cleaved mica surface and left to dry in air at room temperature. Image processing and presentation were done with the help of the user-friendly software Femtoscan 001 (Advanced Technologies Center, Russia).

For the estimation of micelle diameters using AFM data, three different approaches were used, depending on the behavior of the micelles on the surface. The lateral dimensions of the corresponding protrusion measured at half of its height give an overestimated value that is due to the finite probe tip size. The explanation of this broadening effect, conventional in probe microscopy, can be found in ref 68.

For the images in Figures 1b and 2a, where individual micelles were separated from each other and the underlying substrate was clearly seen, the vertical dimensions of the protrusions were taken as the estimated size.

For the samples depicted in Figures 1a and 2b,c, where micelles aggregated in dense layers and vertical dimensions could not be measured correctly, the second approach was used. The mean distance D between the centers of adjacent micelles was taken as the diameter estimation. The details of this estimation are presented in Supporting Information.

The exception was image 2d, which contains micellar aggregates that were strongly deformed on the surface so that their vertical dimensions were close to triblock monolayer thickness. In that case, the diameters of the particles in the solution were evaluated considering the surface area of the micellar aggregates to remain unchanged and using simple geometrical formulas.

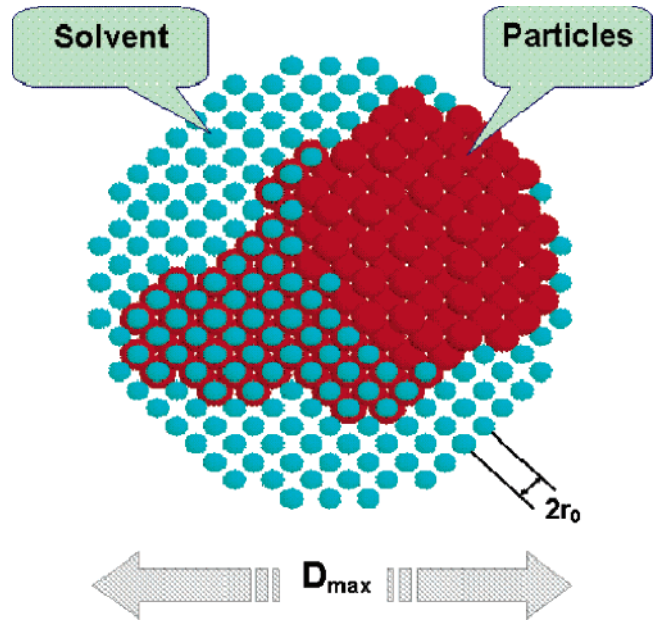
The ASAXS study of the pristine and metal-containing diblock and triblock copolymers (crushed polymer films) was performed at the beamline JUSIFA⁶⁹ on the storage ring DORIS III of the Deutsches Elektronen Synchrotron (DESY, Hamburg) in the range of the momentum transfer $0.4 < s < 7.3 \text{ nm}^{-1}$, where $s = 4\pi(\sin \theta)/\lambda$, 2θ is the scattering angle, and λ is the X-ray wavelength. The samples were measured in a 1-mm-thick aluminum cuvette placed in a vacuum to diminish the parasitic scattering. The scattering profiles were corrected for the background scattering and fluorescence using standard procedures.⁷⁰ The scattering data were collected at different photon energies, $E_0 = 11.482$, $E_1 = 11.530$, $E_2 = 11.550$, and $E_3 = 11.559$ keV. The first energy, being far enough from the L_3 absorption edge of Pt (energy $E = 11.562$ keV corresponding to wavelength $\lambda = 0.107$ nm),^{51,52} was used to study the structure of the pristine copolymers. The anomalous signals, which become considerable in the vicinity of the L_3 , were obtained as the difference in intensities between the scattering curves recorded at the first energy E_0 and those recorded at the successive ones, $I_k(s) = I(s, E_0) - I(s, E_k)$, where $k = 1, 2$, or 3 . These differences are proportional to the anomalous scattering from the Pt atoms described by the scattering length density $\Delta\rho_k = (N_0^2 - N_k^2)e/v_{\text{at}}$, where N_0 and N_k are the numbers of electrons contributing to the scattering far from the resonance (i.e., at the photon energy E_0) and at the energy E_k , respectively, e is the Thompson's radius of the electron, and v_{at} is the atomic volume. Important here is that the anomalous differences correspond to the same population of Pt particles, just with different contrasts, and the proportionality of the difference signals to each other is an additional validation that the signal comes from the Pt particles and not from the matrix. The particle size distribution functions $D_V(R)$ were further computed using an indirect transform program GNOM.⁷¹ Assuming the particles to be spherical, the program solves the integral equation

$$I(s) = (\Delta\rho)^2 \int_{R_{\min}}^{R_{\max}} D_V(R) m^2(R) i_0(sR) dR \quad (1)$$

where R is the radius of a sphere, R_{\min} and R_{\max} are the minimum and maximum radii, respectively, and $i_0(x) = \{[\sin(x) - x \cos(x)]/x^3\}^2$ and $m(R) = (4\pi/3)R^3$ are the sphere form factor and volume, respectively. In the computations of $D_V(R)$, the value of R_{\min} was kept at 0 and that of R_{\max} was selected for each individual data set by successive runs with different values of the parameter. The repeating distances of the periodical motifs in the crystalline regions $\bar{d} = 2\pi/s_{\max}$, corresponding to the peak position s_{\max} on the scattering patterns, were calculated using the program PEAK.⁷¹

The low-resolution shapes of the regions of Pt-nanoparticle localization were reconstructed ab initio from the initial portions of the scattering patterns ($s < 1 \text{ nm}^{-1}$) using the program DAMMIN.^{61,62,71} A sphere of diameter D_{\max} is filled by a regular

SCHEME 1: Principle of the ab Initio Method of Simulated Annealing



grid of K points corresponding to hexagonal packing small spheres (beads or dummy atoms) of radius $r_0 \ll D_{\max}$. The structure of the dummy atoms model (DAM) is defined by a binary configuration vector \mathbf{X}_j , $j = 1, \dots, K$, assigning an index to each bead. The index $X_j = 0$ (or 1) means that the atom does not belong (or belongs) to the volume occupied by Pt nanoparticles within the region of their localization (Scheme 1). The scattering intensity $I(s)$ from the DAM is evaluated as

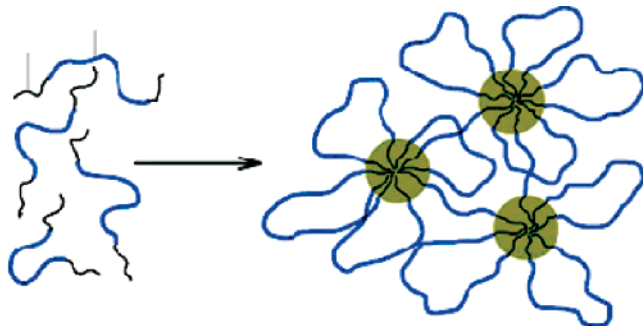
$$I(s) = 2\pi^2 \sum_{l=0}^{\infty} \sum_{m=-l}^l |A_{lm}(s)|^2 \quad (2)$$

where the partial amplitudes $A_{lm}(s)$ are

$$A_{lm}(s) = i^l \sqrt{2/\pi v_a} \sum_j j_l(sr_j) Y_{lm}^*(\omega_j) \quad (3)$$

Here, the sum runs over the dummy atoms with $X_j = 1$, r_j , ω_j as their polar coordinates, $v_a = (4\pi r_0^3/3)/0.74$ is the displaced volume per dummy atom, and $j_l(x)$ and $Y_{lm}(\omega)$ are the spherical Bessel function and the spherical harmonics, respectively. Starting from a random configuration, simulated annealing⁶⁰ is employed to find a compact interconnected configuration X minimizing the discrepancy between the calculated and the experimental curves. In all ab initio calculations, the diameter of the spherical search volume D_{\max} (on average, about 40 nm) was estimated from the analysis of the $p(r)$ functions as evaluated by GNOM.⁷¹ The dummy atoms radii were 1.5–2.0 nm, yielding about $K = 2000$ beads in the search volume. To analyze the stability of the reconstructions, results of about a dozen independent runs were averaged using the program DAMAVER.⁷²

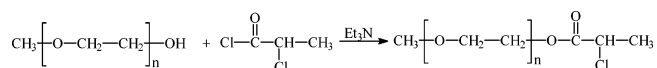
The alternative analysis of the Pt particles formed in the copolymer matrix was performed using the program MIXTURE.⁷³ This program allows one to model mixtures containing up to 10 different components, that is, different types of particles, each characterized by its volume fraction, type of form factor, contrast, type of polydispersity, and potential for interparticle interactions. The experimental scattering pattern

SCHEME 2: Schematic Representation of Triblock P4VP₂₉-*b*-PEO₂₇₃-*b*-P4VP₂₉ Copolymer Micelles


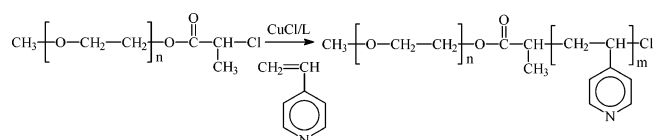
is fitted by a weighted combination of individual curves from the components, and the parameters of the best fit are determined.

Results and Discussion

1. Block Copolymers: Synthesis and Micellization. The synthesis of the diblock PEO₄₅-*b*-P4VP₂₈ and triblock P4VP₂₉-*b*-PEO₂₇₃-*b*-P4VP₂₉ copolymers was carried out using ATRP of 4VP with modified PEO or PEG as the macroinitiators (see Experimental Section). First, PEO or PEG were reacted with halogenated acid chloride to provide the required functionality for ATRP. An example of diblock copolymer formation is given below:



Then this compound was employed in 4VP ATRP using CuCl as a catalyst:



For both block copolymers that are based on P4VP, water is a selective solvent. However, while the PEO-*b*-P2VP becomes molecularly soluble at pH 5.0,⁴⁰ the PEO₄₅-*b*-P4VP₂₈ requires a slightly lower pH (4.5–4.7) for its dissolution. Because in P4VP₂₉-*b*-PEO₂₇₃-*b*-P4VP₂₉ the core-forming blocks are terminal, in aqueous solutions they should form flowerlike micelles,^{74,75} suggesting also a high probability of connections between the micelles as shown in Scheme 2.

Indeed, this block copolymer forms a stable gel at a concentration of 25 g/L, but at lower concentrations, a micellar solution is obtained. Micelles of diblock and triblock copolymers were characterized with AFM. Figure 1a shows a layer of diblock copolymer micelles with a mean diameter of 21 ± 2.5 nm. The micelles do not coalesce despite being deposited from the reaction solution with a concentration of 3 g/L. In contrast, triblock copolymer micelles tend to coalesce, even when the covering of the mica surface is very low (Figure 1b). The estimated mean diameter for these micelles is 22 ± 3 nm. Apparently, despite a much longer PEO block in the triblock copolymer, a similar size of core-forming blocks determines the size of the dried block copolymer micelles. Higher surface coverage for this sample yields scalelike films instead of a micelle monolayer (Figure 1c), suggesting that participation of a triblock copolymer macromolecule in the formation of two micelles facilitates further micelle aggregation.

2. Incorporation of Platinic Acid and Its Reduction: AFM.

As a Pt precursor, we chose platinic acid, H₂PtCl₆·6H₂O, because incorporation of this compound is accompanied by the protonation of pyridine units, facilitating interaction with PtCl₆²⁻ ions resulting from electrostatic attraction. By AFM, interaction of both diblock and triblock PEO-*b*-P4VP copolymer micelles with H₂PtCl₆·6H₂O at a molar ratio of N/Pt = 3:1 yields nearly no changes in micelles measuring 25 ± 4 nm for diblock (Figure 2a) and 23 ± 4 nm for triblock copolymers (Figure 2c). At the same time, incorporation of platinic acid causes even stronger interaction between triblock copolymer micelles: even at a 50-fold dilution of the reaction solution, no individual micelles were observed. Subsequent reduction of micellar solutions with NaBH₄ does not induce any changes in the PEO₄₅-*b*-P4VP₂₈ micelles (a mean diameter is 24 ± 4 nm; Figure 2b), while P4VP₂₉-*b*-PEO₂₇₃-*b*-P4VP₂₉ micelles change dramatically. First, interaction between micelles is suppressed so individual micelles can be easily observed (Figure 2d). In addition, the micelle size increases to 50 ± 10 nm. These facts suggest that (i) each P4VP₂₉-*b*-PEO₂₇₃-*b*-P4VP₂₉ macromolecule is located within a single micelle (flowerlike morphology) and (ii) the aggregation number should increase when the particles are formed. Considering that a pH change and interaction of 4VP units on the Pt-nanoparticle surface are the same for both diblock and triblock copolymer systems, the only difference is likely the suppression of extended PEO chain conformation between micelles favoring formation of individual flowerlike micelles.

3. Micelle Characteristics and Pt-Nanoparticle Formation: TEM and XRD. The metal nanoparticle formation along with the micelle characterization was monitored by TEM. Incorporation of platinic acid in PEO₄₅-*b*-P4VP₂₈ micelles results in a strong interaction between micelles yielding the micelle coalescence (Figure 3a), and the observable micelle diameter is about 12 nm. This value differs from that provided by AFM, suggesting that the TEM image primarily shows a micelle core containing Pt species,⁷⁶ while AFM yields the size of the entire micelle. Indeed, if the P4VP block had a fully extended conformation, the micelle core should have measured about 11.2 nm, which would agree with the TEM data. It is worth mentioning that the P4VP block is pH sensitive; that is, it molecularly dissolves in water at a pH below 4.7 (see above). At the same time, block copolymer micelles loaded with platinic acid do not deteriorate at low pH, similar to PEO-*b*-P2VP micelles reported by us earlier.³⁶ Moreover, the micelle sizes derived from the AFM data stay unchanged, revealing cross-linking of the micelle cores due to complexation with PtCl₆²⁻ ions.

To study the influence of reaction conditions on the particle and micelle sizes, we varied the pH of the reaction medium after platinic acid incorporation. Naturally, the pH is about 2 when the ratio of N to Pt is 3 to 1. To reach a pH of about 10, NaOH was added. In Figure 3b, one can see that the PEO₄₅-*b*-P4VP₂₈ micelles that were reduced at pH = 2 are rather diffuse and ill-defined, tending to form larger aggregates. Evidently, despite an observable micelle core size of 11–13 nm (similar to the H₂PtCl₆-filled micelles), the micelles are loose and tend to aggregate at low pH. At pH = 10, the micelles are better defined, although the sizes discerned from the TEM (where mainly micelle cores are seen) are nearly the same. These micelles are also inclined to aggregate but in a more regular fashion, forming necklacelike (Figure 3c) or wormlike (not shown) micelles. Similar micelle morphologies were reported by us earlier for Au-filled PEO₄₅-*b*-P4VP₂₈.⁴⁴ The Pt nanoparticles formed in these micelles at pH 2 and 10 have mean

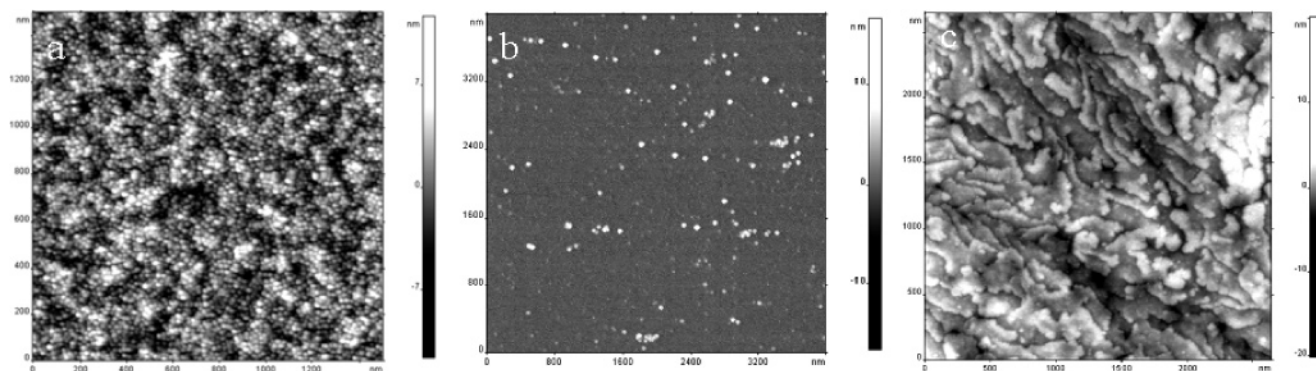


Figure 1. AFM images of PEO₄₅-*b*-P4VP₂₈ (a) and P4VP₂₉-*b*-PEO₂₇₃-*b*-P4VP₂₉ with lower (b) and higher (c) degrees of covering.

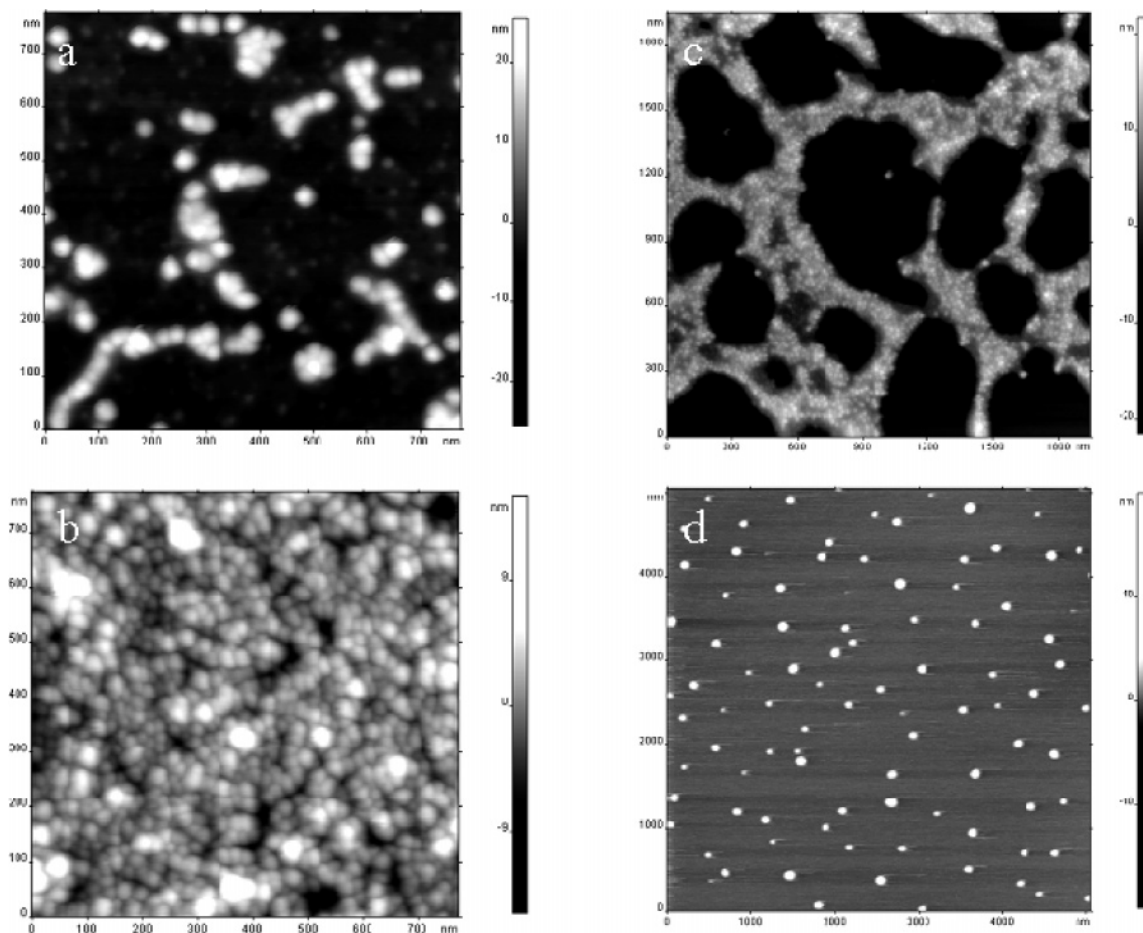


Figure 2. AFM images of PEO₄₅-*b*-P4VP₂₈-H₂PtCl₆ (a), PEO₄₅-*b*-P4VP₂₈-Pt (b), P4VP₂₉-*b*-PEO₂₇₃-*b*-P4VP₂₉-H₂PtCl₆ (c), and P4VP₂₉-*b*-PEO₂₇₃-*b*-P4VP₂₉-Pt (d).

diameters of 1.8 and 1.3 nm, respectively (see Table 1), and their distribution within micelles is different. At pH 10 the nanoparticles are evenly distributed through the micelles (no empty micelles are observed), whereas micelles obtained after Pt-nanoparticle formation at low pH show uneven particle distribution: some micelles look completely empty. We think that, at pH = 10, dense micelle cores allow no exchange between the micelles during particle growth; thus, micelles are evenly filled with nanoparticles. Oppositely, at pH = 2 exchange is facilitated between swollen micelles, so even fast reduction with NaBH₄ results in an uneven distribution of particles within micelles.

The TEM image of P4VP₂₉-*b*-PEO₂₇₃-*b*-P4VP₂₉ micelles filled with platinum acid shows dark circles with diameters of about 14 nm essentially attached to each other (Figure 4a). The

Pt nanoparticles formed after NaBH₄ reduction measure about 2.2 nm (Table 1). They form nanoparticle ensembles (Figure 4b), which should represent the micelle cores. However, the block copolymer phase is practically invisible as a result of low electron density. When the particles are small, they provide an electron contrast to the micelles (similar to staining), while larger nanoparticles do not assist in contrasting the polymer phase. Because the sizes of the particle ensembles differ, this should reflect uneven distribution of nanoparticles in the micelles, but unlike the diblock copolymer, this uneven distribution is observed both in acidic and in basic media. Apparently, restructuring of the micelles during nanoparticle formation facilitates an exchange between micelles and uneven nanoparticle distribution. The largest nanoparticle ensembles measure about 21 nm, confirming the AFM data which shows an in-

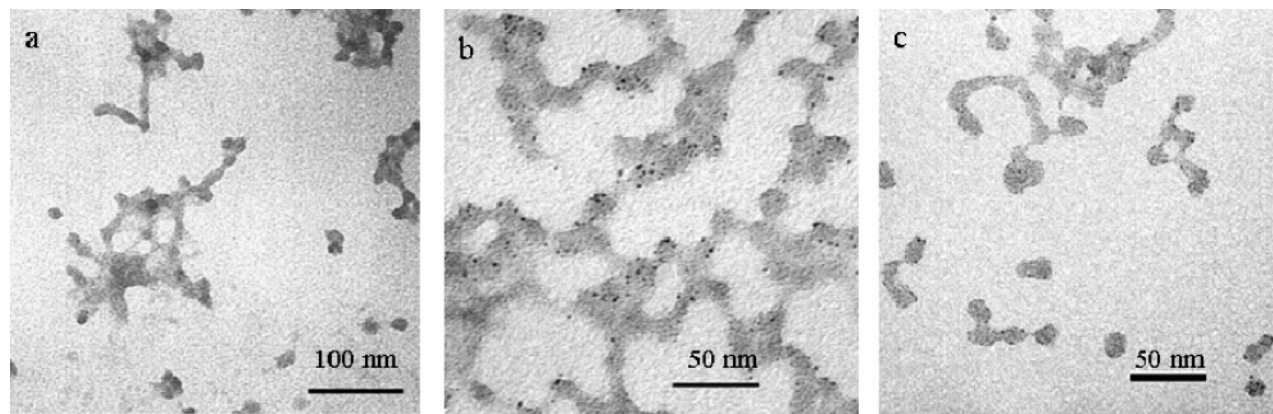


Figure 3. TEM images of PEO₄₅-*b*-P4VP₂₈-H₂PtCl₆ (a) and PEO₄₅-*b*-P4VP₂₈-Pt after NaBH₄ reduction at pH = 2 (b) and pH = 10 (c).

TABLE 1: Characteristics of Pt Nanoparticles Obtained from XRD, TEM, and SAXS Data

block copolymer	sample no. and reduction conditions	$d_{\text{XRD}},^a$ nm	$d_{\text{TEM}},^b$ nm	$d_{\text{ASAXS}}^1,^c$ nm	$d_{\text{ASAXS}}^2,^d$ nm	R_g
PEO ₄₅ - <i>b</i> -P4VP ₂₈	1; pH = 2, NaBH ₄	2.0	1.8 ± 0.3	1.6		16.2
	2; pH = 10, NaBH ₄ + N ₂ H ₄	amorphous	1.4 ± 0.4			
	3; pH = 10, N ₂ H ₄ + NaBH ₄	3.1	1.3 ± 0.3	2.1		17.3
	4; pH = 10, NaBH ₄	amorphous	1.3 ± 0.2	1.7		17.2
	5; pH = 10, N ₂ H ₄	5.4	2.6 ± 0.4	2.5	40	17.0
P4VP ₂₉ - <i>b</i> -PEO ₂₇₃ - <i>b</i> -P4VP ₂₉	6; pH = 2, NaBH ₄	2.8	2.2 ± 0.3	2.2	20	9.8
	7; pH = 10, NaBH ₄ + N ₂ H ₄	3.5	2.5 ± 0.3	3.1	40	19.3
	8; pH = 10, N ₂ H ₄ + NaBH ₄	3.0	2.2 ± 0.4			
	9; pH = 10, NaBH ₄	2.4	2.7 ± 0.4	2.5		17.8
	10; pH = 10, N ₂ H ₄	6.3	2.0 ± 0.3	2.2	40	19.3

^a Mean Pt-nanoparticle diameter obtained from XRD data. ^b Mean Pt-nanoparticle diameter obtained from TEM (100 nanoparticles were calculated). ^c Mean Pt-nanoparticle diameter from ASAXS data; square deviation is 0.4 nm. ^d Mean diameter of Pt-particle ensembles from ASAXS data.

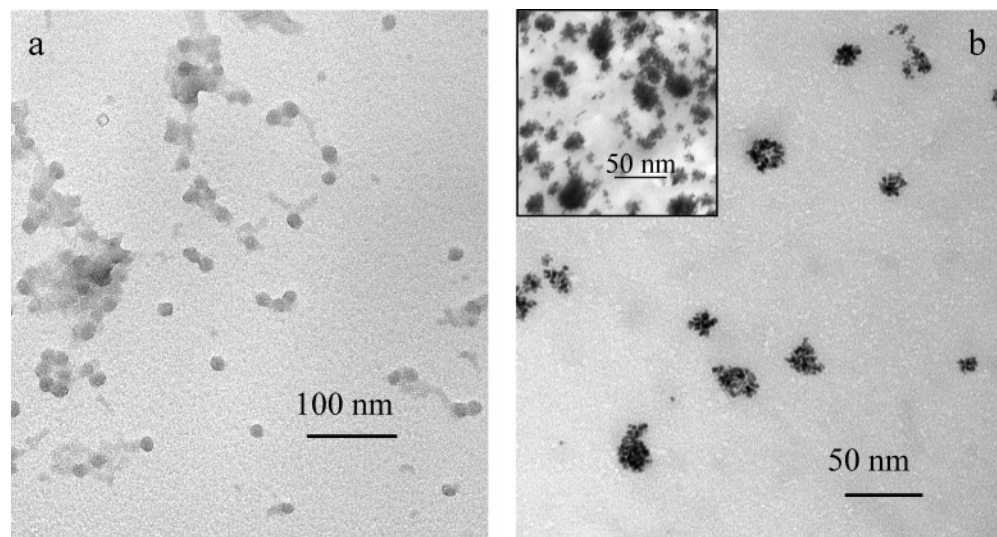


Figure 4. TEM images of P4VP₂₉-*b*-PEO₂₇₃-*b*-P4VP₂₉-H₂PtCl₆ (a) and P4VP₂₉-*b*-PEO₂₇₃-*b*-P4VP₂₉-Pt after NaBH₄ reduction at pH = 2 (b). Inset in b shows the cross section of the same sample obtained by imbedding the powder (crushed bulk film) in epoxy resin.

crease of P4VP₂₉-*b*-PEO₂₇₃-*b*-P4VP₂₉ micelles after nanoparticle formation.

It is noteworthy that, for the majority of the samples (with nos. 1 and 9 from Table 1 the only exceptions), the nanoparticle diameters obtained from the XRD data are larger than those obtained from the TEM images. This could be due to the presence of a small fraction of larger particles that are not detected with TEM. Another possible reason for this discrepancy is an amorphous character of the small Pt nanoparticles (note that, for sample nos. 2 and 4, no crystalline phase was detected). A comparison of the TEM and XRD data with those obtained from ASAXS (see section 4.2) will allow us to further clarify this issue. In general, amorphous Pt nanoparticles are rarely

observed,^{77,78} although as recently reported, amorphization may be associated with an energy gain.⁷⁹ We believe that, in our case, a strong interaction between the Pt species and the 4VP units may prevent the formation of the crystalline phase.

For pH 10, further variations of reduction conditions were explored. Normally, the use of different reducing agents with a different nucleation rate allows one to change the nanoparticle characteristics and morphology. In particular, fast-acting reducing agents yield small particles, while sluggish reducing agents give large particles.²³ In this work, we explored the possibility of combining two reducing agents of different strengths and compared the results with those for individual reducing agents. We assumed that if only 30% of the Pt atoms are nucleated

with NaBH_4 (fast reducing agent), a limited amount of nuclei should be formed. If the further reduction is directed by a sluggish reducing agent ($\text{N}_2\text{H}_4 \cdot \text{H}_2\text{O}$), the larger particles should grow. The opposite addition order of the reducing agents should lead to a different morphology. One could expect two populations of particles: the larger ones nucleated by $\text{N}_2\text{H}_4 \cdot \text{H}_2\text{O}$ and the smaller ones nucleated by the further addition of NaBH_4 . However, from Table 1, one can see that, for both block copolymer systems, the latter case does not result in broader particle distribution, while the former case does not yield larger particles. In general, independently of the reducing agent, larger particles grow in the triblock copolymer micelles than in diblock micelles; this can be attributed to an easier exchange between the micelles in the former case. Apparently, only reduction with hydrazine hydrate (sluggish reducing agent) leads to larger particles in the diblock copolymer micelles, while in triblock copolymer micelles, the Pt nanoparticles are even smaller after hydrazine reduction than in some other cases. In our earlier work we observed that the nanoparticle size does not depend on the reducing agent type when nanoparticles grow in a confined environment^{57,80} or when a strong interaction between the polymer matrix and the growing nanoparticles in the strongly cross-linked environment overpowers kinetically controlled nucleation and growth.⁵⁸ Here, we present the first example when a similar mechanism is observed for the block copolymer micelles, and it should be attributed to a strong interaction between the vinyl pyridine units and the growing nanoparticle surface in the micelle cores cross-linked with platinumic acid (when nucleation is slow, more “cross-links” remain unchanged in the course of the reduction resembling conditions of ref 58).

4. ASAXS Investigation of Diblock and Triblock Copolymers Containing Pt Nanoparticles. ASAXS was applied to study particle size distributions of Pt nanoparticles embedded in the $\text{PEO}_{45}\text{-}b\text{-P4VP}_{28}$ and $\text{P4VP}_{29}\text{-}b\text{-PEO}_{273}\text{-P4VP}_{29}$ micelles. The use of ASAXS allows one to accurately determine the influence of the reducing agent type, pH, and polymer structure on the size distributions of the metal nanoparticles formed in the block copolymer micelles. As the measurements have been performed on powders acquired by crushing the films obtained after water evaporation from the micellar solutions, the location of the nanoparticles was directly analyzed in bulk block copolymers.

4.1. Scattering Profiles. The experimental scattering profiles from both systems, measured at the beam energy far from the Pt absorption edge, are displayed in Figure 5. The observed central scattering points to the presence of nanoscale structural heterogeneities in all samples, including pristine block copolymers (Figure 5a,b, curve 1). In the latter case, the central scattering can be explained by a microphase separation of block copolymers in the bulk.^{81,82} After incorporation inside the micelle core occurs, platinumic acid may form clusters, as discussed in our preceding papers,^{59,80} and these clusters further contribute to the central maximum.

Moreover, some of the scattering patterns that occur after platinumic acid incorporation (Figure 5a, curves 2 and 3) display shoulders or weak maxima pointing to the formation of weakly ordered quasi-crystalline structures. The positions and amplitudes of these peaks depend on the chemical composition and pH of the block copolymer systems. When platinumic acid is incorporated in block copolymer micelles, it serves as a cross-linking agent for the block copolymer cores, which influences the microphase segregation in the bulk after the evaporation of water and leads to a partial self-ordering in the samples compared to that of the pristine block copolymers. The

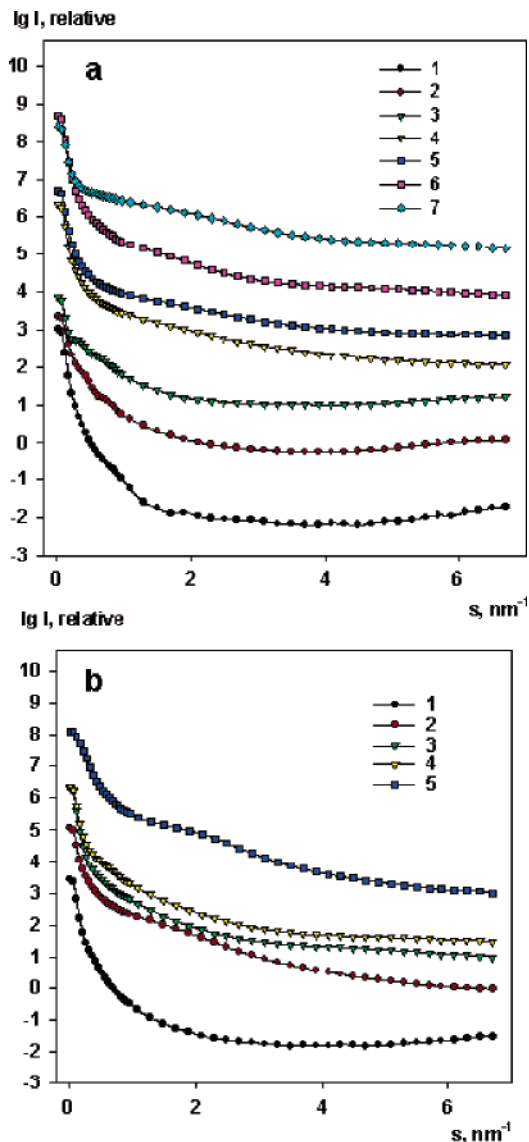


Figure 5. ASAXS profiles from $\text{PEO}_{45}\text{-}b\text{-P4VP}_{28}$ (a) and $\text{P4VP}_{29}\text{-}b\text{-PEO}_{273}\text{-}b\text{-P4VP}_{29}$ (b) copolymers. In part a: curve 1 is from $\text{PEO}_{45}\text{-}b\text{-P4VP}_{28}$, pristine; curve 2 is from $\text{PEO}_{45}\text{-}b\text{-P4VP}_{28}\text{-H}_2\text{PtCl}_6$ at pH 10; curve 3 is from $\text{PEO}_{45}\text{-}b\text{-P4VP}_{28}\text{-H}_2\text{PtCl}_6$ at pH 2; curve 4 is from $\text{PEO}_{45}\text{-}b\text{-P4VP}_{28}\text{-Pt}$ at pH 10, reduced with NaBH_4 ; curve 5 is from $\text{PEO}_{45}\text{-}b\text{-P4VP}_{28}\text{-Pt}$ at pH 10, reduced with NaBH_4 and N_2H_4 ; curve 6 is from $\text{PEO}_{45}\text{-}b\text{-P4VP}_{28}\text{-Pt}$ at pH 10, reduced with N_2H_4 ; curve 7 is from $\text{PEO}_{45}\text{-}b\text{-P4VP}_{28}\text{-Pt}$ at pH 2, reduced with NaBH_4 . In part b: curve 1 is from $\text{P4VP}_{29}\text{-}b\text{-PEO}_{273}\text{-}b\text{-P4VP}_{29}$, pristine; curve 2 is from $\text{P4VP}_{29}\text{-}b\text{-PEO}_{273}\text{-}b\text{-P4VP}_{29}\text{-Pt}$ at pH 10, reduced with NaBH_4 ; curve 3 is from $\text{P4VP}_{29}\text{-}b\text{-PEO}_{273}\text{-}b\text{-P4VP}_{29}\text{-Pt}$ at pH 10, reduced with NaBH_4 and N_2H_4 ; curve 4 is from $\text{P4VP}_{29}\text{-}b\text{-PEO}_{273}\text{-}b\text{-P4VP}_{29}\text{-Pt}$ at pH 10, reduced with N_2H_4 ; curve 5 is from $\text{P4VP}_{29}\text{-}b\text{-PEO}_{273}\text{-}b\text{-P4VP}_{29}\text{-Pt}$ at pH 2, reduced with NaBH_4 .

incorporation of platinumic acid in the diblock copolymer, bringing the pH of the reaction solution to 2, results in two weak maxima at 0.2 and 0.5 nm^{-1} (Figure 5a, curve 2), corresponding to periodicities of about 30 and 12 nm, respectively. When the pH is adjusted to 10, after the platinumic acid loading, the peaks for the bulk sample appear at 0.3 and 0.6 (Figure 5a, curve 3), that is, a periodicity of about 20 and 10 nm. The equidistant peak positions suggest a lamellar ordering in the system at pH 10. The ordering at pH 2 appears to be more complicated and cannot be determined from the available data. Comparison of these results with TEM and AFM data suggests that both for pH 2 and for pH 10, the larger periodicity is close to the micelle size while the shorter period matches the micelle core size.

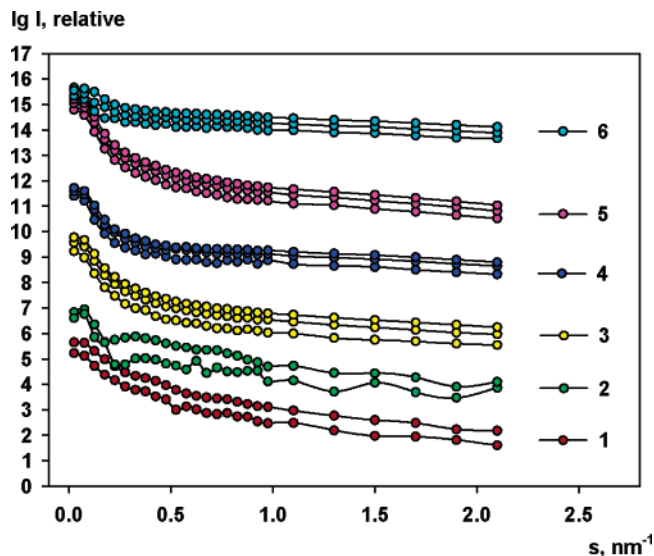


Figure 6. Difference ASAXS data (anomalous signal) from the Pt-containing PEO₄₅-*b*-P4VP₂₈ copolymer: curve 1 is from PEO₄₅-*b*-P4VP₂₈-H₂PtCl₆ at pH 10; curve 2 is from PEO₄₅-*b*-P4VP₂₈-H₂PtCl₆ at pH 2; curve 3 is from PEO₄₅-*b*-P4VP₂₈-Pt at pH 10, reduced with NaBH₄; curve 4 is from PEO₄₅-*b*-P4VP₂₈-Pt at pH 10, reduced with NaBH₄ and N₂H₄; curve 5 is from PEO₄₅-*b*-P4VP₂₈-Pt at pH 10, reduced with N₂H₄; curve 6 is from PEO₄₅-*b*-P4VP₂₈-Pt at pH 2, reduced with NaBH₄. The successive groups of curves are displaced one logarithmic unit down for better visualization. For each sample, the three differences are between the measured intensity far from the absorption edge and those near the edge $I(s, E_0) - I(s, E_i)$ as described in the Characterization section. Exceptions are PEO₄₅-*b*-P4VP₂₈-H₂PtCl₆ at pH 10 and 2, where the anomalous difference for the first energy E_1 near the edge was not reliable.

Apparently, cross-linking of the cores with platinum acid results in preservation of the micelle core sizes when the micellar solution is evaporated to obtain bulk material.

After the reduction of the Pt ions and the formation of the metal nanoparticles, the maxima in the scattering profiles disappeared, pointing to the further loss of order in the internal structure of the copolymer matrix (quantitative characterization of the reorganized structures in the absence of maxima is no longer possible). Here, an interaction of the core-forming block with nanoparticles should occur as a result of the adsorption of pyridine units on the nanoparticle surface. However, this kind of interaction may involve fewer pyridine units than the interaction with platinum acid, so the micelle core containing the nanoparticles is easier to reshape when the bulk material is formed.

4.2. Particle Size Distributions. PEO₄₅-*b*-P4VP₂₈. To obtain the scattering from the Pt-containing particles, differences between the SAXS intensities at different energies were calculated. Analyzing the energy dependence allows the separation of particle and polymer matrix contributions. Figure 6 demonstrates the sets of difference curves between the scattering profiles at the first energy and those at the three successive energies.

Most of the differences (three for each sample) are proportional to the expected anomalous signal. The only exception is the diblock copolymer containing platinum acid at two different pHs (Figure 6, curve sets 1 and 2), where only two difference curves were meaningful. The particle size distributions computed by GNOM for the diblock copolymer systems are presented in Figure 7. The profiles for Pt-containing clusters (curves 1 and 2 were multiplied by a factor of 10 for better visualization) reveal the major relatively broad fraction of the clusters with

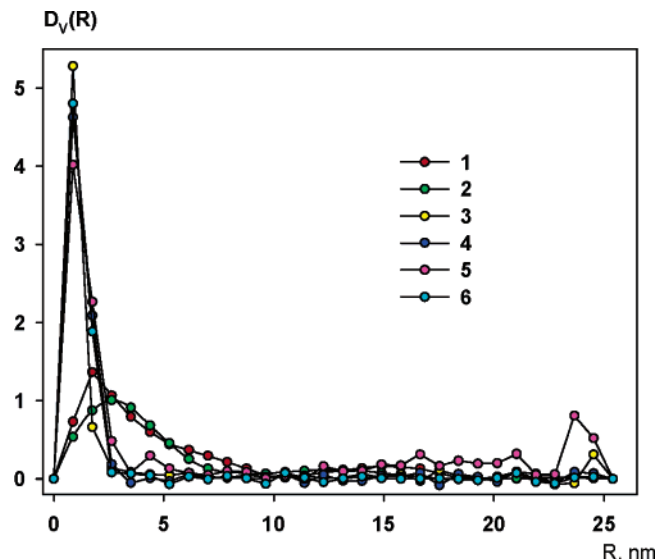


Figure 7. Volume distribution functions of the Pt nanoparticles in PEO₄₅-*b*-P4VP₂₈ copolymer. The numbering of the distributions and colors of the symbols correspond to those in Figure 6.

the average radius of about 2.5 nm. After the reduction of the Pt ions, the magnitude of the distribution functions increases compared to that of the H₂PtCl₆ clusters as a result of higher contrast of the metal particles, and the distributions become rather narrow with a maximum at about $R = 1$ nm (Table 1). Some larger particles are present in smaller amounts. The exception is the Pt-containing sample reduced by the sluggish reducing agent N₂H₄ at pH 10, which contains a distinct fraction of large particles with radii of more than 20 nm (Figure 7, curve 6). Our results indicate that the influence of the initial pH on the particle formation is negligible for this system. A decrease in the Pt-nanoparticle size compared to that of the platinum acid cluster size is consistent with an increase of the Pt-metal density so platinum acid clusters serve as nuclei for Pt-nanoparticle formation.

P4VP₂₉-*b*-PEO₂₇₃-P4VP₂₉. Figures 8 and 9 present anomalous signals for the triblock copolymer system and particle size distribution functions, respectively. The distributions have a major fraction of small particles with a radius of about 1 nm (Table 1), and nearly all the samples contain some amount of large particles (note that scattering from the large particles is significantly more intense than that from small particles, so even a small fraction of large particles yield a noticeable contribution to the scattering profiles). Only the sample with the Pt particles obtained after a NaBH₄ reduction at pH 10 (Figure 9, curve 1) displays a practically monomodal distribution profile without the larger particles. Interestingly, the reduction by the same reducing agent at pH 2 leads to the formation of a broad fraction of large particles displaying a maximum at $R = 10$ nm (Figure 9, curve 4). The reduction with hydrazine hydrate and with a sequential addition of hydrazine hydrate and sodium borohydride yields yet larger particles with R of about 20 nm (Figure 9, curves 2 and 3). Because neither TEM nor XRD reveals the large particles, one may assume that these larger scatterers (with diameters of ~ 20 to 40 nm) are polymer nanostructures filled with Pt species (see the next sections). A similar phenomenon was discussed in our preceding paper.⁵⁹

Comparison of the Diblock and the Triblock Copolymer Systems. For comparison, the average Pt particle sizes were computed from the distribution functions obtained for the two copolymer systems. The distributions calculated from the three anomalous differences were computed independently for each

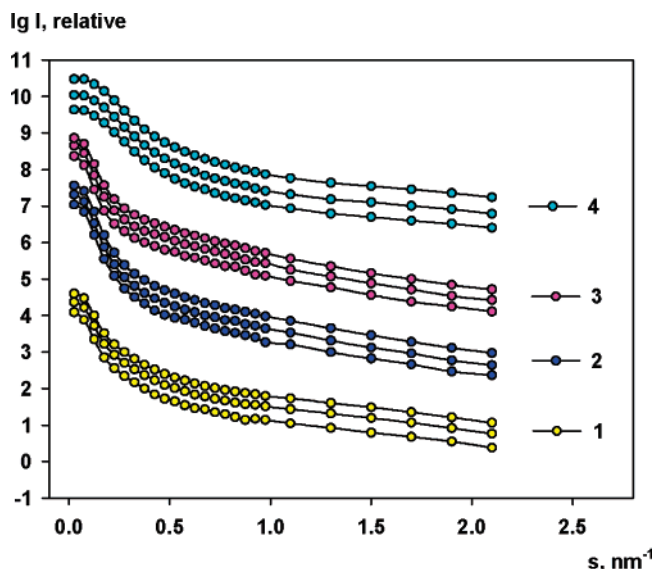


Figure 8. Difference ASAXS data (anomalous signal) from the Pt-containing P4VP₂₉-*b*-PEO₂₇₃-*b*-P4VP₂₉ copolymer: curve 1 is from 4VP₂₉-*b*-PEO₂₇₃-*b*-P4VP₂₉-Pt at pH 10, reduced with NaBH₄; curve 2 is from P4VP₂₉-*b*-PEO₂₇₃-*b*-P4VP₂₉-Pt at pH 10, reduced with NaBH₄ and N₂H₄; curve 3 is from P4VP₂₉-*b*-PEO₂₇₃-*b*-P4VP₂₉-Pt at pH 10, reduced with N₂H₄; curve 4 is from P4VP₂₉-*b*-PEO₂₇₃-*b*-P4VP₂₉-Pt at pH 2, reduced with NaBH₄. The successive curves are displaced one logarithmic unit down for better visualization. For each sample, differences were calculated using scattering profiles recorded at different energies (see Figure 6).

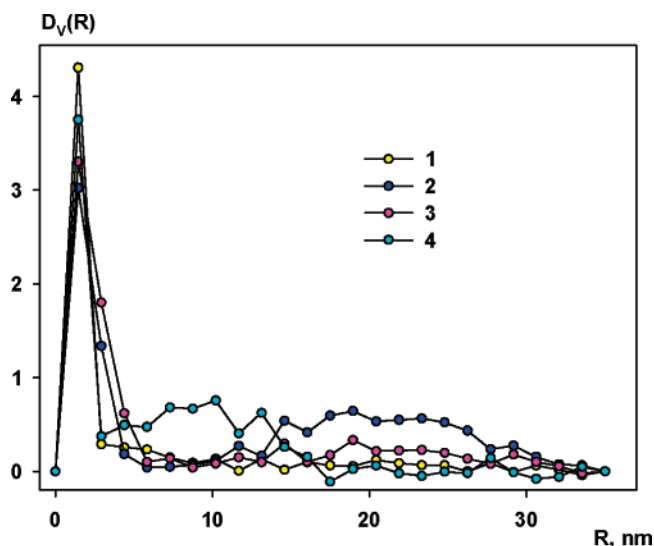


Figure 9. Volume distribution functions of the Pt nanoparticles in the P4VP₂₉-*b*-PEO₂₇₃-*b*-P4VP₂₉ copolymer. The numbering of the distributions and colors of the symbols correspond to those in Figure 8.

sample, and the value of R_{\max} in GNOM calculations⁷¹ was varied as described in Experimental Section. The average data presented in Table 1 indicate that Pt nanoparticles prepared in PEO₄₅-*b*-P4VP₂₈ micelles are systematically smaller than those in P4VP₂₉-*b*-PEO₂₇₃-P4VP₂₉ micelles: $d_{\text{ASAXS}}^1 = (1.5-2.5) \pm 0.4$ nm for diblock copolymers and $d_{\text{ASAXS}}^1 = (2.0-3.0) \pm 0.4$ nm for triblock copolymers. This result is in good agreement with the TEM data.

Overall, formation of Pt nanoparticles in PEO₄₅-*b*-P4VP₂₈ and P4VP₂₉-*b*-PEO₂₇₃-P4VP₂₉ copolymers reveals both common features and clear differences. First, all the samples contain major fractions of small particles with the maximum at about $R = 1$ nm, independent of the polymer matrix, the pH, and the

reducing agent type. Second, reduction with sluggish hydrazine hydrate always leads to a bimodal profile of the volume distribution function independently of polymer systems and pH conditions, whereas the fast reducing agent (NaBH₄) yields different results for different systems. Third, the distribution functions for the P4VP₂₉-*b*-PEO₂₇₃-P4VP₂₉ system are broader than those for diblock copolymers. This observation can be explained by the facilitated intermicellar exchange for the triblock copolymers as compared with that of the diblock copolymers. Last, all the samples contain a certain amount of large particles and, thus, yield relatively high values of the radii of gyration. The reason is that the experimental radius of gyration, R_g , of a polydisperse system is biased toward the large particles being a z average

$$\langle R_g^2 \rangle_z = \int_0^\infty R_g^2(R) D_V(R) R^6 dR / \int_0^\infty D_V(R) R^6 dR = \int_0^\infty R_g^2(R) D_V(R) R^6 dR / \langle R^6 \rangle$$

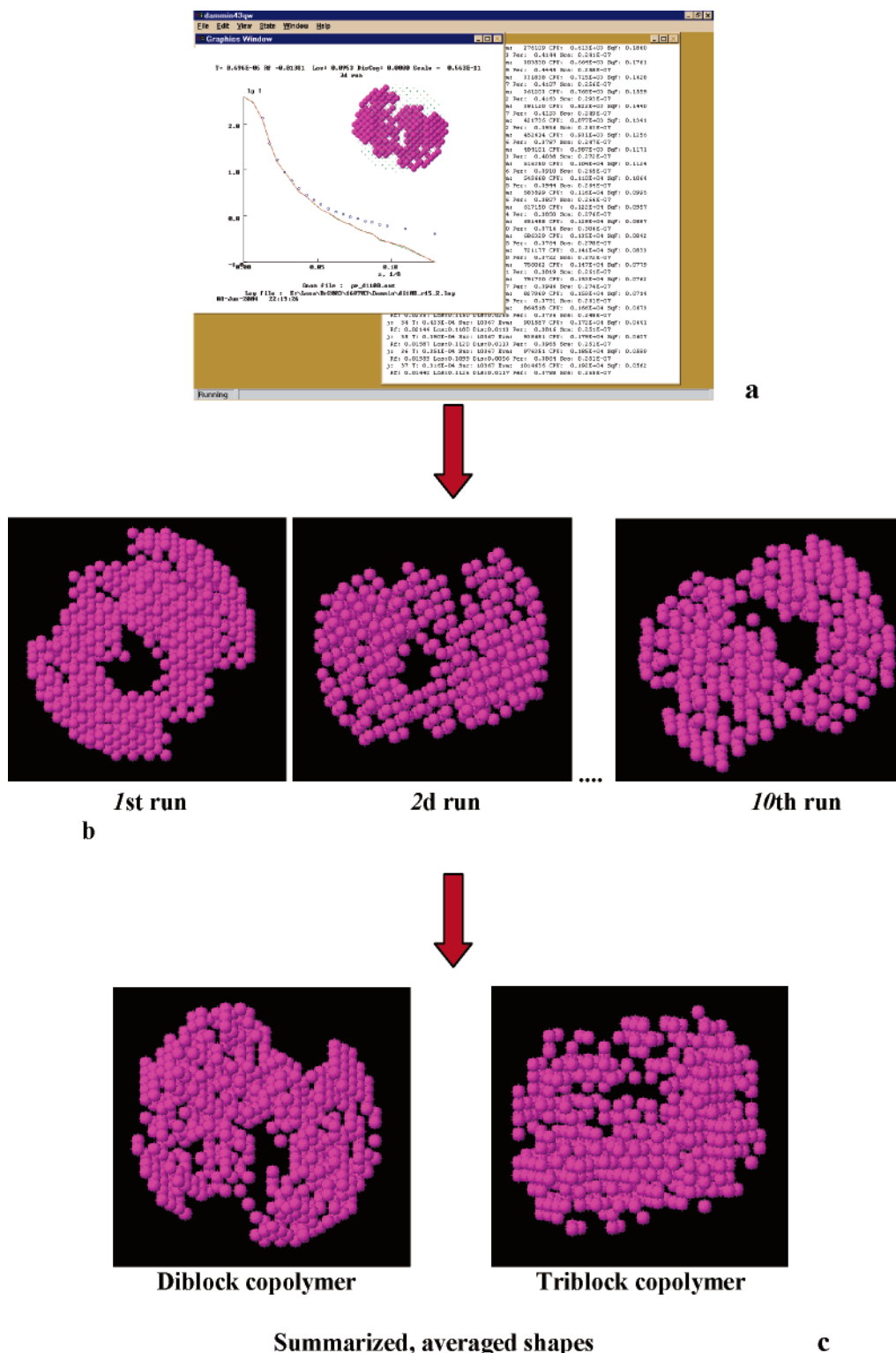
(for polydisperse spheres $\langle R_g^2 \rangle_z = 3\langle R^8 \rangle / 5\langle R^6 \rangle$). As one can see from Table 1, the experimental R_g values exceed 16 nm, reflecting this bias. The only exception is the sample P4VP₂₉-*b*-PEO₂₇₃-P4VP₂₉ after a NaBH₄ reduction at pH 2, which displays no maximum at 10 or 20 nm, leading to the mean R_g value of 9.8 nm. Generally, for PEO₄₅-*b*-P4VP₂₈, the amount of large particles seems to be negligible with the exception of the Pt-containing sample reduced by the sluggish reducing agent N₂H₄, but almost all triblock copolymer samples contain a larger number of particles with sizes of about 40 nm. These large particles are attributed to polymer regions filled with Pt nanoparticles, the scattering of which occurs as the scattering of individual Pt-containing structures.^{58,59}

Interestingly, for all the samples, the particle diameters obtained from XRD are systematically larger than those from ASAXS. Because both methods, unlike TEM, provide an average over large numbers of particles, the observed difference indicates that the smaller Pt particles in the ensembles are amorphous. The amorphous particles are detected by ASAXS but not by XRD, thus, leading to smaller effective sizes provided by the former method.

4.3. Shape Reconstruction of the Regions Containing Pt Nanoparticles. An attempt was further made to reconstruct the low-resolution Pt-particle shapes from the ASAXS data using the ab initio simulated annealing procedure.⁶⁰⁻⁶² The nanoscale structure is represented by a set of densely packed beads of two kinds, matrix and particle, as in Scheme 1. The shape, in terms of the beads belonging to the particle, is obtained by fitting the experimental data without a priori information, except for the maximum size of the object (R_{\max}) as calculated by the program GNOM.⁷¹ In principle, this approach is valid for systems of identical particles but, under certain conditions, can also be used for polydisperse systems. In this particular case, the use of the ab initio method can be justified by the TEM data, showing the rather homogeneous populations of Pt-containing micelles in all the samples.

The simulated annealing method was applied to the difference ASAXS data, and independent reconstructions were averaged as described in Experimental Section (see Scheme 3). The radius of the beads representing the shape of the Pt-rich aggregates was selected to be 1 nm, that is, the average radius of the small Pt particles. For both copolymer systems and in all conditions of nanoparticle formation, slightly oblate hollow shapes were obtained (a typical shape is displayed in Scheme 3c). These hollow bodies have the following average diameters: diblock

SCHEME 3: Computation of Shape Models of PEO₄₅-*b*-P4VP₂₈ and P4VP₂₉-*b*-PEO₂₇₃-*b*-P4VP₂₉ Copolymers for the Screen Shot of the *n*th Run of the Computations (a), the Accumulation of the Intermediate Models (b), and the Averaged Shapes (c)

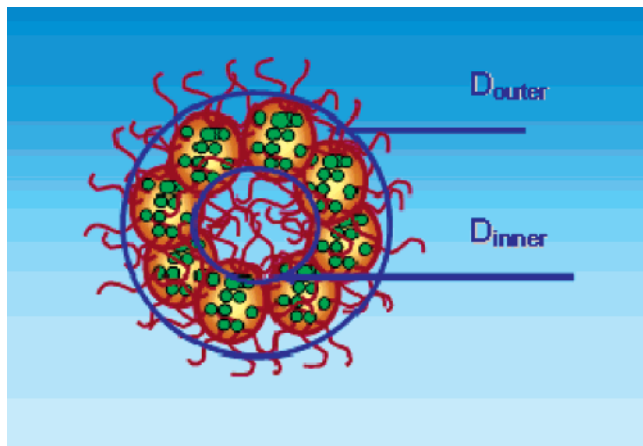


copolymers, $D_{\text{outer}} \approx 40 \pm 5$ nm, $D_{\text{inner}} \approx 25 \pm 5$ nm; triblock copolymers, $D_{\text{outer}} \approx 45 \pm 5$ nm, $D_{\text{inner}} \approx 25 \pm 5$ nm.

Given the low resolution of the reconstruction, the thickness of the spherical layer is about $h = (D_{\text{outer}} - D_{\text{inner}})/2 = 7\text{--}12$ nm for both systems, which is in agreement with the sizes of the micelle cores as determined by TEM. Moreover, the sizes of the spheroids approximating the shapes of the regions of the nanoparticle localization coincide with those of the larger

scatterers in the size distribution functions in Figures 7 and 9 (maxima at $R = 20$ nm). As the shapes deduced from the anomalous signal reflect the distribution of the pure Pt aggregates in the system and are not sensitive to the scattering from the polymer phase, the following model of the overall organization of the Pt-containing micelles in the bulk can be suggested. The micelle cores, with sizes of about 10 nm, aggregate to form slightly oblate hollow bodies with an outer

SCHEME 4: Model of the Micelle Organization in the PEO₄₅-*b*-P4VP₂₈ and P4VP₂₉-*b*-PEO₂₇₃-*b*-P4VP₂₉ Copolymers in the Bulk



diameter of about 40 nm (Scheme 4); the center of the spheroid is filled with a PEO block, while the Pt particles are located at its periphery. This result is particularly valuable because no such detailed structural information can be obtained from TEM. As can be seen from the inset to Figure 4b, showing a cross section of the triblock copolymer sample with Pt nanoparticles embedded in the epoxy resin, nanoparticle distribution in the bulk looks very similar to that of the micelles dried on the carbon-coated grid, but no details can be discerned. Thus, ASAXS provides important structural information which cannot be obtained from other techniques.

The above model of the Pt-rich clusters consists of small particles forming large aggregates, that is, two types of objects with distinctly different dimensions. The scattering from the entire system should be a sum of the scattering contributions from the two types of particles, and this model can be further verified using an alternative fitting by the program MIXTURE (see Experimental Section). The two particle types were small solid spheres and large spheres with two variable densities in a concentric core and shell, and both types of particles could be polydispersed (Gaussian distribution). The best fits to the experimental data (not shown) were provided by a mixture of fairly monodisperse (10%) small particles with $R \approx 1$ nm and large particles with R of about 20 nm, an outer-shell thickness of about 8 nm, and a ratio of shell to core density of about 2:1. These results further corroborate the ab initio model in Scheme 4 and also the data obtained by TEM and XRD.

Conclusions

We synthesized diblock PEO₄₅-*b*-P4VP₂₈ and triblock P4VP₂₉-*b*-PEO₂₇₃-*b*-P4VP₂₉ copolymers using ATRP of 4VP with modified PEO or PEG as macroinitiators and analyzed the structural organization of these block copolymer micelles during their metalation with a Pt species using a combination of AFM, XRD, TEM, and ASAXS as complementary techniques.

By AFM, the interaction of both diblock and triblock copolymer micelles with H₂PtCl₆·6H₂O at a molar ratio N/Pt = 3:1 yields nearly no changes in the micelles measuring 25 ± 4 nm for diblock and 23 ± 4 nm for triblock copolymers, yet a stronger interaction between triblock copolymer micelles is observed. A subsequent reduction of micellar solutions with NaBH₄ does not induce any changes in the PEO₄₅-*b*-P4VP₂₈ micelles, while P4VP₂₉-*b*-PEO₂₇₃-*b*-P4VP₂₉ micelles dramatically increase in size (to 50 ± 10 nm), suggesting that each P4VP₂₉-*b*-PEO₂₇₃-*b*-P4VP₂₉ macromolecule is located within a

single micelle (flowerlike morphology). From TEM, the observable micelle core size for diblock copolymer micelles after Pt-nanoparticle formation is in the range 11–13 nm.

For most samples, the diameters of the Pt nanoparticles obtained from XRD data are larger than those obtained from TEM images. This could be due to the presence of a small fraction of larger particles that are not detected with TEM and/or due to the amorphous character of small Pt nanoparticles. The comparison with the ASAXS data on particle sizes confirms the latter suggestion. Yet, the particle size is practically independent of the type of reducing agent, resembling a “cage” effect that was observed by us earlier.⁸⁰ This can be attributed to a strong interaction between the vinyl pyridine units and the growing nanoparticle surface in the micelle cores cross-linked with platonic acid.

Shape simulation of the regions containing nanoparticles showed that spherical micelle cores, with sizes of about 10 nm, aggregate forming slightly oblate hollow bodies with an outer diameter of about 40 nm. Apparently, the Pt-deficient interior of these spheroids is filled by the PEO phase.

A contribution from each applied method of structural characterization allowed us to reconstruct a general picture of the metalation of diblock PEO₄₅-*b*-P4VP₂₈ and triblock P4VP₂₉-*b*-PEO₂₇₃-*b*-P4VP₂₉ copolymers and to offer the entire model of the copolymer configurations containing Pt nanoparticles.

Acknowledgment. We sincerely thank NATO Science for Peace Programme (SfP-974173) and Russian Foundation for Basic Research (Grant RFBR-04-03-32928) for financial support of this research. We would like to acknowledge the HASYLAB (DESY, Hamburg) for providing the beam time at JUSIFA beamline and Dr. G. Goerigk for assistance in the anomalous scattering measurements and data processing.

Supporting Information Available: Estimation of D from the AFM data. This material is available free of charge via the Internet at <http://pubs.acs.org>.

References and Notes

- Hamley, I. U. *The Physics of Block Copolymers*; Oxford University Press: Oxford, U.K., 1998.
- Foerster, S.; Antonietti, M. *Adv. Mater.* **1998**, *10*, 195–217.
- Hadjichristidis, N.; Pispas, S.; Floudas, G. A. *Block Copolymers Synthetic Strategies, Physical Properties, and Applications*; John Wiley & Sons: Hoboken, NJ, 2003.
- Raez, J.; Tomba, J. P.; Manners, I.; Winnik, M. A. *J. Am. Chem. Soc.* **2003**, *125*, 9546–9547.
- Cao, L.; Manners, I.; Winnik, M. A. *Macromolecules* **2002**, *35*, 8258–8260.
- Yan, X.; Liu, F.; Li, Z.; Liu, G. *Macromolecules* **2001**, *34*, 9112–9116.
- Ding, J.; Liu, G.; Yang, M. *Polymer* **1997**, *38*, 5497–5501.
- Seregina, M. V.; Bronstein, L. M.; Platonova, O. A.; Chernyshov, D. M.; Valetsky, P. M.; Hartmann, J.; Wenz, E.; Antonietti, M. *Chem. Mater.* **1997**, *9*, 923–931.
- Bronstein, L. M.; Chernyshov, D. M.; Volkov, I. O.; Ezernitskaya, M. G.; Valetsky, P. M.; Matveeva, V. G.; Sulman, E. M. *J. Catal.* **2000**, *196*, 302–314.
- Klingelhöfer, S.; Heitz, W.; Greiner, A.; Oestreich, S.; Förster, S.; Antonietti, M. *J. Am. Chem. Soc.* **1997**, *119*, 10116.
- Mayer, A. B. R.; Mark, J. E. *Colloid Polym. Sci.* **1997**, *275*, 333–340.
- Jaramillo, T. F.; Baek, S.-H.; Cuenya, B. R.; McFarland, E. W. *J. Am. Chem. Soc.* **2003**, *125*, 7148–7149.
- Platonova, O. A.; Bronstein, L. M.; Solodovnikov, S. P.; Yanovskaya, I. M.; Obolonkova, E. S.; Valetsky, P. M.; Wenz, E.; Antonietti, M. *Colloid Polym. Sci.* **1997**, *275*, 426–431.
- Rutnakornpituk, M.; Thompson, M. S.; Harris, L. A.; Farmer, K. E.; Esker, A. R.; Riffle, J. S.; Connolly, J.; St. Pierre, T. G. *Polymer* **2002**, *43*, 2337–2348.
- Diana, F. S.; Lee, S.-H.; Petroff, P. M.; Kramer, E. J. *Nano Lett.* **2003**, *3*, 891–895.

- (16) Kane, R. S.; Cohen, R. E.; Silbey, R. *Chem. Mater.* **1999**, *11*, 90.
- (17) Leppert, V. J.; Murali, A. K.; Risbud, S. H.; Stender, M.; Power, P. P.; Nelson, C.; Banerjee, P.; Mayes, A. M. *Philos. Mag. B* **2002**, *82*, 1047–1054.
- (18) Spatz, J. P.; Herzog, T.; Mössmer, S.; Ziemann, P.; Möller, M. *Adv. Mater.* **1999**, *11*, 149.
- (19) Loginova, T. P.; Kabachii, Y. A.; Sidorov, S. N.; Zhirov, D. N.; Valetsky, P. M.; Ezernitskaya, M. G.; Dybrovina, L. V.; Bragina, T. P.; Lependina, O. L.; Stein, B.; Bronstein, L. M. *Chem. Mater.* **2004**, *16*, 2369–2378.
- (20) Jeong, B.; Bae, Y. H.; Lee, D. S.; Kim, S. W. *Nature* **1997**, *388* (6645), 860–862.
- (21) Otsuka, H.; Nagasaki, Y.; Kataoka, K. *Adv. Drug Delivery Rev.* **2003**, *55*, 403–419.
- (22) Antonietti, M.; Henz, S. *Nachr. Chem., Tech. Lab.* **1992**, *40*, 308–314.
- (23) Antonietti, M.; Wenz, E.; Bronstein, L.; Seregina, M. *Adv. Mater.* **1995**, *7*, 1000–1005.
- (24) Spatz, J. P.; Roescher, A.; Möller, M. *Adv. Mater.* **1996**, *8*, 337–340.
- (25) Moffitt, M.; McMahon, L.; Pessel, V.; Eisenberg, A. *Chem. Mater.* **1995**, *7*, 1185–1192.
- (26) Saito, R.; Okamura, S.; Ishizu, K. *Polymer* **1993**, *34*, 1189–1195.
- (27) Boontongkong, Y.; Cohen, R. E. *Macromolecules* **2002**, *35*, 3647–3652.
- (28) Underhill, R. S.; Liu, G. *Chem. Mater.* **2000**, *12*, 2082–2091.
- (29) Lu, Z.; Liu, G.; Phillips, H.; Hill, J. M.; Chang, J.; Kydd, R. A. *Nano Lett.* **2001**, *1*, 683–687.
- (30) Yan, X.; Liu, G.; Liu, F.; Tang, B. Z.; Peng, H.; Pakhomov, A. B.; Wong, C. Y. *Angew. Chem., Int. Ed.* **2001**, *40*, 3593–3596.
- (31) Edrington, A. C.; Urbas, A. M.; DeRege, P.; Chen, C. X.; Swager, T. M.; Hadjichristidis, N.; Xenidou, M.; Fetters, L. J.; Joannopoulos, J. D.; Fink, Y.; Thomas, E. L. *Adv. Mater.* **2001**, *13*, 421–425.
- (32) Tadd, E. H.; Bradley, J.; Tannenbaum, R. *Langmuir* **2002**, *18*, 2378–2384.
- (33) Park, C.; Yoon, J.; Thomas, E. L. *Polymer* **2003**, *44*, 6725–6760.
- (34) Abes, J. I.; Cohen, R. E.; Ross, C. A. *Chem. Mater.* **2003**, *15*, 1125–1131.
- (35) Bennett, R. D.; Xiong, G. Y.; Ren, Z. F.; Cohen, R. E. *Chem. Mater.* **2004**, *16*, 5589–5595.
- (36) Bronstein, L. M.; Sidorov, S. N.; Valetsky, P. M.; Hartmann, J.; Coelfen, H.; Antonietti, M. *Langmuir* **1999**, *15*, 6256–6262.
- (37) Bronstein, L.; Kraemer, E.; Berton, B.; Burger, C.; Foerster, S.; Antonietti, M. *Chem. Mater.* **1999**, *11*, 1402–1405.
- (38) Gohy, J.-F.; Willet, N.; Varshney, S.; Zhang, J.-X.; Jerome, R. *Angew. Chem., Int. Ed.* **2001**, *40*, 3214–3216.
- (39) Bailey, L.; Vamvakaki, M.; Billingham, N. C.; Armes, S. P. *Polym. Prepr. (Am. Chem. Soc., Div. Polym. Chem.)* **1999**, *40* (2), 263–264.
- (40) Martin, T. J.; Prochazka, K.; Munk, P.; Webber, S. E. *Macromolecules* **1996**, *29*, 6071–6073.
- (41) Moffitt, M.; Vali, H.; Eisenberg, A. *Chem. Mater.* **1998**, *10*, 1021–1028.
- (42) Antonietti, M.; Wenz, E.; Bronstein, L.; Seregina, M. *Adv. Mater.* **1995**, *7*, 1000–1005.
- (43) Mayer, A. B. R.; Mark, J. E. *Eur. Polym. J.* **1998**, *34*, 103–108.
- (44) Sidorov, S. N.; Bronstein, L. M.; Kabachii, Y. A.; Valetsky, P. M.; Soo, P. L.; Maysinger, D.; Eisenberg, A. *Langmuir* **2004**, *20*, 3543–3550.
- (45) Dembo, A. T.; Yakunin, A. N.; Zaitsev, V. S.; Mironov, A. V.; Starodubtsev, S. G.; Khokhlov, A. R.; Chu, B. J. *Polym. Sci., Part B: Polym. Phys.* **1996**, *34*, 2893.
- (46) Svergun, D. I.; Shtykova, E. V.; Dembo, A. T.; Bronstein, L. M.; Platonova, O. A.; Yakunin, A. N.; Valetsky, P. M.; Khokhlov, A. R. *J. Chem. Phys.* **1998**, *109*, 11109–11116.
- (47) Bronstein, L. M.; Platonova, O. A.; Yakunin, A. N.; Yanovskaya, I. M.; Valetsky, P. M.; Dembo, A. T.; Obolonkova, E. S.; Makhaeva, E. E.; Mironov, A. V.; Khokhlov, A. R. *Colloids Surf., A* **1999**, *147*, 221.
- (48) Bronstein, L. M.; Platonova, O. A.; Yakunin, A. N.; Yanovskaya, I. M.; Valetsky, P. M.; Dembo, A. T.; Makhaeva, E. E.; Mironov, A. V.; Khokhlov, A. R. *Langmuir* **1998**, *14*, 252–259.
- (49) Shtykova, E. V.; Dembo, A. T.; Makhaeva, E. E.; Khokhlov, A. R.; Evmenenko, G. V.; Reynaers, H. *Langmuir* **2000**, *16*, 5284.
- (50) Feigin, L. A.; Svergun, D. I. *Structure Analysis by Small-Angle X-ray and Neutron Scattering*; Plenum Press: New York, 1987.
- (51) Stuhmann, H. B.; Goerigk, G.; Munk, B. In *Handbook on Synchrotron Radiation*; Rubenstein, E., Ebashi, S., Koch, M., Eds.; Elsevier: Amsterdam, The Netherlands, 1994; p 555.
- (52) Haubold, H.-G.; Gebhardt, R.; Buth, G.; Goerigk, G. In *Resonant Anomalous X-ray Scattering*; Materlik, G., Sparks, C. J., Fischer, K., Eds.; Elsevier Science: Oxford, U.K., 1994; pp 295–304.
- (53) Vad, T.; Hajbolouri, F.; Haubold, H.-G.; Scherer, G. G.; Wokaun, A. *J. Phys. Chem. B* **2004**, *108*, 12442–12449.
- (54) Dingenouts, N.; Patel, M.; Rosenfeldt, S.; Pontoni, D.; Narayanan, T.; Ballauff, M. *Macromolecules* **2004**, *37*, 8152–8159.
- (55) Brumberger, H.; Hagrman, D.; Goodisman, J.; Finkelstein, K. D. *J. Appl. Crystallogr.* **2005**, *38*, 147–151.
- (56) Svergun, D. I.; Shtykova, E. V.; Kozin, M. B.; Volkov, V. V.; Dembo, A. T.; Shtykova, E. V. J.; Bronstein, L. M.; Platonova, O. A.; Yakunin, A. N.; Valetsky, P. M.; Khokhlov, A. R. *J. Phys. Chem. B* **2000**, *104*, 5242.
- (57) Svergun, D. I.; Kozin, M. B.; Konarev, P. V.; Shtykova, E. V.; Volkov, V. V.; Chernyshov, D. M.; Valetsky, P. M.; Bronstein, L. M. *Chem. Mater.* **2000**, *12*, 3552.
- (58) Bronstein, L. M.; Linton, C.; Karlinsey, R.; Ashcraft, E.; Stein, B.; Svergun, D. I.; Kozin, M.; Khotina, I. A.; Spontak, R. J.; Werner-Zwanziger, U.; Zwanziger, J. W. *Langmuir* **2003**, *19*, 7071–7083.
- (59) Shtykova, E. V.; Svergun, D. I.; Chernyshov, D. M.; Khotina, I. A.; Valetsky, P. M.; Spontak, R. J.; Bronstein, L. M. *J. Phys. Chem. B* **2004**, *108*, 6175–6185.
- (60) Kirkpatrick, S.; Gelatt, C. D., Jr.; Vecchi, M. P. *Science* **1983**, *220*, 671.
- (61) Svergun, D. I. *Biophys. J.* **1999**, *76*, 2879.
- (62) Svergun, D. I.; Becirevic, A.; Schrempf, H.; Koch, M. H. J.; Grueber, G. *Biochemistry* **2000**, *39*, 10677.
- (63) Shtykova, E. V.; Shtykova, E. V., Jr.; Volkov, V. V.; Konarev, P. V.; Dembo, A. T.; Makhaeva, E. E.; Ronova, I. A.; Khokhlov, A. R.; Reynaers, H.; Svergun, D. I. *J. Appl. Crystallogr.* **2003**, *36*, 669–673.
- (64) Volkov, V. V.; Lapuk, V. A.; Kayushina, R. L.; Shtykova, E. V.; Varlamova, E. Y.; Malfois, M.; Svergun, D. I. *J. Appl. Crystallogr.* **2003**, *36*, 503–508.
- (65) Ciampolini, M.; Nardi, N. *Inorg. Chem.* **1966**, *5*, 41–44.
- (66) Jankova, K.; Chen, X.; Kops, J.; Batsberg, W. *Macromolecules* **1998**, *31*, 538–541.
- (67) Xia, J.; Zhang, K.; Matyjaszewski, K. *Macromolecules* **1999**, *32*, 3531–3533.
- (68) Stemmer, A.; Engel, A. *Ultramicroscopy* **1990**, *34*, 129–140.
- (69) Haubold, H.-G.; Gruenhagen, K.; Wagener, M.; Jungbluth, H.; Heer, H.; Pfeil, A.; Rongen, H.; Brandenburg, G.; Moeller, R.; Matzerath, J.; Hiller, P.; Halling, H. *Rev. Sci. Instrum.* **1989**, *60*, 1943.
- (70) EMBL website. <http://www.embl-hamburg.de/ExternalInfo/Research/Sax> (for program descriptions).
- (71) Svergun, D. I. *J. Appl. Crystallogr.* **1992**, *25*, 495–503.
- (72) Volkov, V. V.; Svergun, D. I. *J. Appl. Crystallogr.* **2003**, *36*, 860–864.
- (73) Konarev, P. V.; Volkov, V. V.; Sokolova, A. V.; Koch, M. H. J.; Svergun, D. I. *J. Appl. Crystallogr.* **2003**, *36*, 1277–1282.
- (74) Zhou, Z.; Chu, B.; Peiffer, D. G. *Langmuir* **1995**, *11*, 1956–1965.
- (75) Maiti, S.; Chatterji, P. R. *J. Phys. Chem. B* **2000**, *104*, 10253–10257.
- (76) Moffitt, M.; Eisenberg, A. *Macromolecules* **1997**, *30*, 4363–4373.
- (77) Ko, H. Y. Y.; Mizuhata, M.; Kajinami, A.; Deki, S. *J. Mater. Chem.* **2002**, *12*, 1495–1499.
- (78) Inkson, B. J.; Dehm, G.; Wagner, T. *J. Microsc. (Oxford, U.K.)* **2004**, *214*, 252–260.
- (79) Apra, E.; Baletto, F.; Ferrando, R.; Fortunelli, A. *Phys. Rev. Lett.* **2004**, *93*, 065502.
- (80) Bronstein, L. M.; Chernyshov, D. M.; Valetsky, P. M.; Wilder, E. A.; Spontak, R. J. *Langmuir* **2000**, *16*, 8221.
- (81) Hajduk, D. A.; Gruner, S. M.; Rangarajan, P.; Register, R. A.; Fetters, L. J.; Honeker, C.; Albalak, R. J.; Thomas, E. L. *Macromolecules* **1994**, *27*, 490–501.
- (82) Ludwigs, S.; Boker, A.; Abetz, V.; Müller, A. H. E.; Krausch, G. *Polymer* **2003**, *44*, 6815–6823.